

# Supporting Information

## for

# Crystal Facet Engineering of Spinel NiCo<sub>2</sub>O<sub>4</sub> with Enhanced Activity and Water Resistance for Tuneable Catalytic Methane Oxidation

*Yash Boyjoo<sup>a,b,c</sup>, Yonggang Jin<sup>a,\*</sup>, Xin Mao<sup>d</sup>, Guangyu Zhao<sup>a</sup>, Thomas Gengenbach<sup>e</sup>, Aijun Du<sup>d</sup>, Hua Guo<sup>a,\*</sup>, Jian Liu<sup>b,f,\*</sup>*

<sup>a</sup>CSIRO Mineral Resources, 1 Technology Court, Pullenvale, QLD 4069, Australia

<sup>b</sup>State Key Laboratory of Catalysis, Dalian Institute of Chemical Physics, Chinese Academy of Sciences, 457 Zhongshan Road, Dalian 116023, China

<sup>c</sup>Curtin Mauritius, Telfair, Moka, Mauritius

<sup>d</sup>School of Chemistry, Physics and Mechanical Engineering, Queensland University of Technology, Brisbane, QLD 4001, Australia

<sup>e</sup>CSIRO Manufacturing, Bayview Avenue, Clayton, VIC 3168, Australia

<sup>f</sup>DICP-Surrey Joint Centre for Future Materials, Department of Chemical and Process Engineering and Advanced Technology Institute, University of Surrey, Guildford, Surrey, GU2 7XH, UK

\* Corresponding authors' emails: [jian.liu@surrey.ac.uk](mailto:jian.liu@surrey.ac.uk), [yonggang.jin@csiro.au](mailto:yonggang.jin@csiro.au)  
[hua.guo@csiro.au](mailto:hua.guo@csiro.au)

## 1. Experimental Section

### 1.1 Materials

Cobalt nitrate hexahydrate  $\text{Co}(\text{NO}_3)_2 \cdot 6\text{H}_2\text{O}$ , nickel nitrate hexahydrate  $\text{Ni}(\text{NO}_3)_2 \cdot 6\text{H}_2\text{O}$ , polyvinylpyrrolidone (PVP,  $M_R = 55,000$ ), hexamethylenetetramine (HMT), sodium hydroxide (NaOH) and absolute ethanol were purchased from Sigma-Aldrich.

### 1.2 Method

The procedure for the synthesis of 111- $\text{NiCo}_2\text{O}_4$  and 112- $\text{NiCo}_2\text{O}_4$  were according to previously reported method <sup>1</sup> with modification.

To synthesise  $\text{NiCo}_2\text{O}_4$  nanoplates with  $\{1\ 1\ 2\}$  exposed crystal facets (112- $\text{NiCo}_2\text{O}_4$ -X, where X is the calcination temperature), 6 mmol  $\text{Co}(\text{NO}_3)_2 \cdot 6\text{H}_2\text{O}$  and 3 mmol  $\text{Ni}(\text{NO}_3)_2 \cdot 6\text{H}_2\text{O}$  were dissolved in 60 mL DI water. Thereafter, 3 mmol HMT dissolved in 60 mL DI water was added to the mixture under continuous stirring at room temperature. The solution was allowed to mix for 30 min after which the pH was adjusted to 10 by adding 1 M NaOH dropwise. The obtained green suspension was stirred for 2 h and was then transferred to a Teflon-lined autoclave for heating in an oven at 120 °C for 24 h. Once cooled, the solid product was washed thoroughly with DI water several times, collected by centrifugation and dried at 60 °C. Finally, the dried product was calcined at different temperatures (400, 450 and 500 °C) for 3 h (heating rate of 5 °C  $\text{min}^{-1}$ ) in a tube furnace under air flow.

To synthesise  $\text{NiCo}_2\text{O}_4$  nanoplates with  $\{1\ 1\ 1\}$  exposed crystal facets (111- $\text{NiCo}_2\text{O}_4$ -X, where X is the calcination temperature), 11.2 mmol  $\text{Co}(\text{NO}_3)_2 \cdot 6\text{H}_2\text{O}$  and 5.6 mmol  $\text{Ni}(\text{NO}_3)_2 \cdot 6\text{H}_2\text{O}$  were dissolved in 40 mL mixed solvent (water to ethanol volume ratio of 1:1). 4 g of PVP was then added to the solution and the mixture was stirred for 30 min at room temperature to allow for complete dissolution. Then 100 mL of 0.4 M NaOH solution was added dropwise to form a blue suspension. The suspension was transferred to a Teflon-lined autoclave that was heated in an oven at 120 °C for 15 h. Once cooled, the solid product was washed thoroughly with DI water and acetone several times, collected by centrifugation and dried at 60

°C. Finally, the dried product was calcined at different temperatures (400 and 450 °C) for 3 h (heating rate of 5 °C min<sup>-1</sup>) in a tube furnace under air flow.

### 1.3 Characterisation

X-ray diffraction (XRD) patterns were collected at room temperature on a Panalytical Empyrean diffractometer with Co K $\alpha$  radiation ( $\lambda=1.78901$  Å) over the  $2\theta$  range of 10-80 °. Scanning electron microscopy (SEM) images were taken using a Quanta 200F produced by FEI Company. Scanning transmission electron microscopy (STEM) images were acquired using a JEM-ARM200F with energy-dispersive X-ray spectroscopy. The porous properties of the catalysts including the specific surface area were measured by N<sub>2</sub> adsorption at 77K using a volumetric gas adsorption analyser (Micrometrics ASAP2020). Prior to analysis, the samples were degassed at 150 °C overnight. Temperature programmed reduction (TPR) with hydrogen (H<sub>2</sub>-TPR) and methane (CH<sub>4</sub>-TPR) were conducted on a catalyst characterization analyzer (Microtrac BELCAT II) equipped with a thermal conductivity detector (TCD) and a mass spectrometer (MS) for hydrogen and methane measurement. Prior to the H<sub>2</sub>-TPR analysis, 10 mg of catalyst was placed in a quartz micro-reactor located in a furnace, and pre-treated with oxygen (10 vol% O<sub>2</sub> in Ar with a total flow rate of 40 ml/min) at 250 °C for 1 h. Reduction of sample by hydrogen was carried out in a H<sub>2</sub>/Ar stream (10 vol% of H<sub>2</sub>), with a total flow rate of 40 ml/min and a linear heating rate of 10 °C /min in the temperature range of 60–800 °C. For CH<sub>4</sub>-TPR analysis, 40 mg of catalyst was pre-treated under the same pretreatment conditions of H<sub>2</sub>-TPR, followed by reacting with methane by feeding a CH<sub>4</sub>/Ar stream (10% vol% of CH<sub>4</sub>) with a total flow rate of 20 ml/min in the temperature range of 60–800 °C.

X-ray photoelectron spectroscopy (XPS) analysis was performed using an AXIS Nova spectrometer (Kratos Analytical Inc., Manchester, UK) with a monochromated Al K $\alpha$  source at a power of 180 W (15 kV, 12 mA), a hemispherical analyser operating in the fixed analyser transmission mode and the standard aperture (analysis area: 0.3 mm  $\times$  0.7 mm). The total pressure in the main vacuum chamber during analysis was typically between 10<sup>-9</sup> and 10<sup>-8</sup> mbar.

Survey spectra were acquired at a pass energy of 160 eV and step size of 0.5 eV. To obtain more detailed information about chemical structure, oxidation states etc., high resolution spectra were recorded from individual peaks at 40 eV pass energy and step size of 0.1 eV (full width at half maximum of Ag 3d<sub>5/2</sub> peak < 0.8 eV, typical peak width for polymers < 0.9 eV). The samples were filled into shallow wells of a custom-built sample holder and were analysed at a nominal photoelectron emission angle of 0° with respect to the surface normal. Since the actual emission angle is ill-defined in the case of particles and powders (ranging from 0° to 90°) the sampling depth may range from 0 nm to approx. 10 nm. Data processing was performed using CasaXPS processing software version 2.3.25 (Casa Software Ltd., Teignmouth, UK). All elements present were identified from survey spectra. The atomic concentrations of the detected elements were calculated using integral peak intensities and the sensitivity factors supplied by the manufacturer. Peak fitting was employed for three reasons: 1. to aid with elemental quantification (subtraction of Ni LMM Auger peak from the Co 2p spectral region before quantifying Co 2p), 2. to estimate the contributions of NiO and Ni(OH)<sub>2</sub> to Ni 2p spectra, and 3. to quantify contributions from chemically different species to the C 1s and O 1s spectra. A three-parameter Tougaard background was subtracted from the relevant spectral regions. As fit components we used either analytical functions (Voigt line shape) or model components derived from reference compounds. Appropriate constraints were applied to all components to ensure acceptable and meaningful fitting results.

The accuracy associated with quantitative XPS is ca. 10% - 15%.

Precision (i.e., reproducibility) depends on the signal/noise ratio but is usually much better than 5%. The latter is relevant when comparing similar samples.

#### **1.4 Methane catalytic oxidation tests**

Methane catalytic oxidation experiments were performed in a U-shaped quartz tube fixed-bed reactor with inner diameter of 6 mm. The tests were carried out at atmospheric pressure. 40 mg of the catalyst was loaded into the reactor and supported by quartz wool. A

mixed reaction gas containing 0.7 vol % CH<sub>4</sub>, 15.0 vol % O<sub>2</sub> and balance Ar was flowed through the catalyst bed at a flow rate of 20 mL min<sup>-1</sup>, corresponding to a gas hourly space velocity of 40000 mL h<sup>-1</sup> g<sup>-1</sup>. For tests under humid conditions, the gas was passed through water at 25 °C which saturated the gas mixture with water vapour at 3.2% concentration. Prior to the catalytic tests, the catalyst was pre-treated under the reaction atmosphere for 1 h at 250 °C and then cooled down to 150 °C until the temperature was stable. Then the CH<sub>4</sub> catalytic oxidation performance was evaluated by heating the catalyst bed at 5 °C min<sup>-1</sup> up to 500 °C. The composition of the gas at the outlet was monitored on-line using a quadrupole mass spectrometer (Hidden MS HPR20) with a secondary electron multiplier detector. MS signal with mass/charge (m/z) ratio of 15 was used to monitor methane concentration. The methane percent conversion was calculated as:

$$\frac{(\text{influent concentration of } CH_4 - \text{effluent concentration of } CH_4)}{\text{influent concentration of } CH_4} \times 100$$

Apart from CO<sub>2</sub>, no other carbon containing compounds were found in the gas effluent and as a result, the product selectivity to CO<sub>2</sub> for all catalyst samples was 99.99%.

## 2. Theoretical calculations

Density functional theory as implemented in the Vienna Ab-initio Simulation Package (VASP) was employed to optimize the geometry structures<sup>2, 3</sup>. The exchange-correlation interactions were described by the generalized gradient approximation (GGA)<sup>4</sup> in the form of the Perdew-Burke-Ernzerhof functional (PBE)<sup>5</sup>. A cut-off energy of 500 eV for plain-wave basis sets was adopted and the convergence threshold was 10<sup>-5</sup> eV, and 5×10<sup>-3</sup> eV/Å for energy and force, respectively. The weak interaction was described by DFT+D3 method using empirical correction in Grimme's scheme<sup>6</sup>. The vacuum space was set to be more than 15 Å, which was enough to avoid the interaction between periodical images. The reaction Gibbs free energy changes ( $\Delta G$ ) for each elementary steps were based on the computational hydrogen electrode model, which can be calculated by the following equation;

$$\Delta G = \Delta E + \Delta ZPE - T\Delta S$$

where  $\Delta E$  represents energy difference obtained from DFT calculations,  $\Delta ZPE$  is the change of zero-point energies (ZPE), T is the temperature of 298.15K, and  $\Delta S$  is the change in entropy of products and reactants.

The minimum energy pathway for transition state search was determined by using a climbing image nudged elastic band method (CINEB).<sup>7,8</sup>

### 3. Supporting Figures and Tables

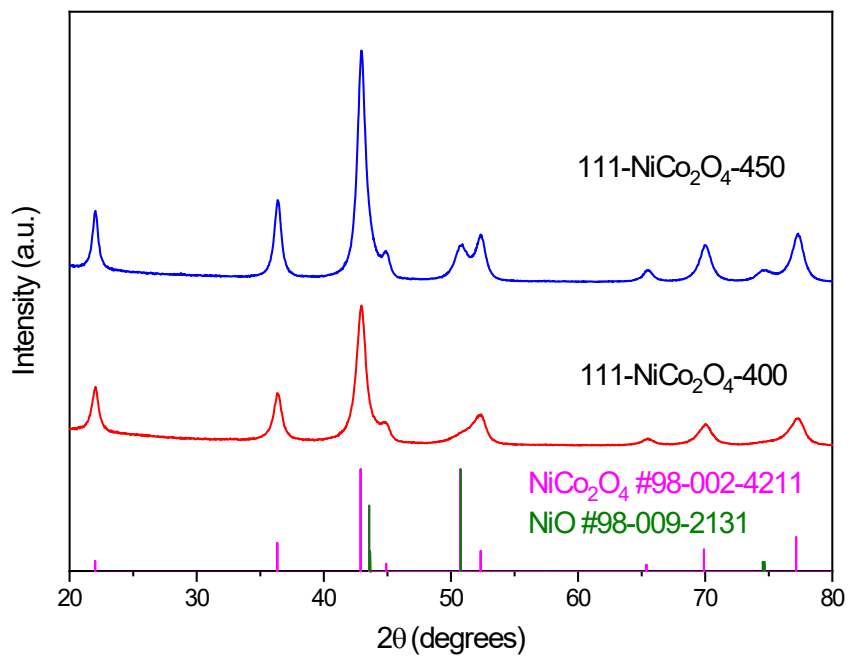


**Fig. S1** XRD patterns of 111-NiCo<sub>2</sub>O<sub>4</sub> calcined at different temperatures.

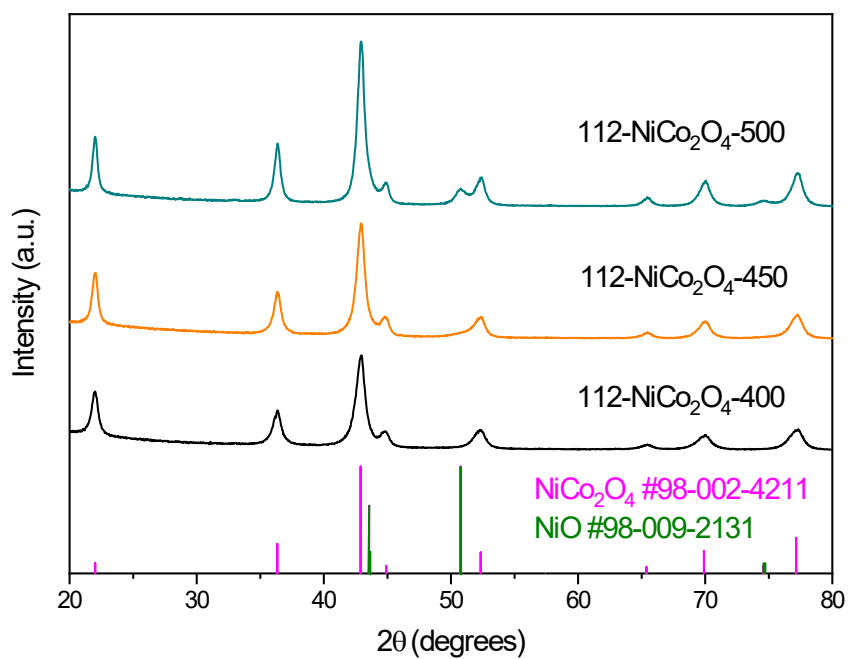


**Fig. S2** XRD patterns of 112-NiCo<sub>2</sub>O<sub>4</sub> calcined at different temperatures.

Please note that in this case, XRD could not be used to detect the preferentially exposed facets of 111-NiCo<sub>2</sub>O<sub>4</sub> and 112-NiCo<sub>2</sub>O<sub>4</sub>, possibly due to the already large peak heights collected from the samples. Similar results were observed for spinel samples in other works<sup>1,9</sup>.

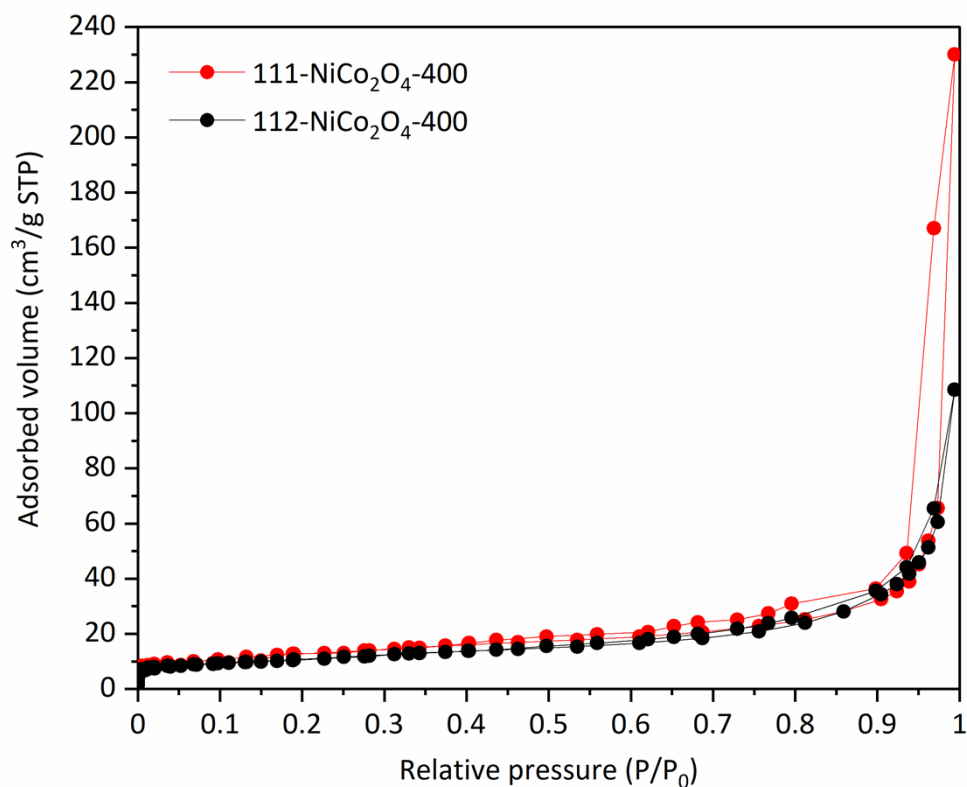


**Fig. S3** N<sub>2</sub> adsorption isotherm for 111-NiCo<sub>2</sub>O<sub>4</sub>-400 and 112-NiCo<sub>2</sub>O<sub>4</sub>-400.

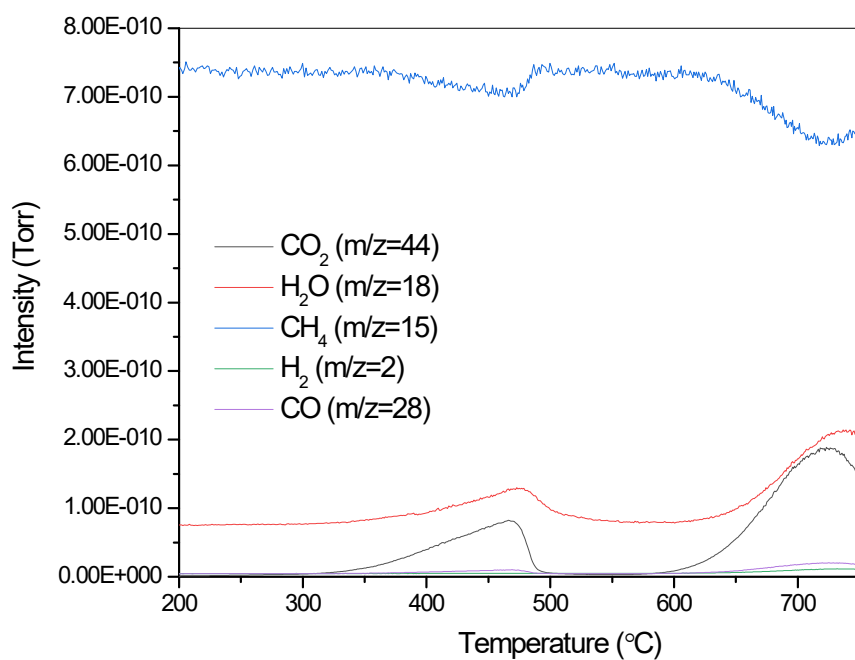


**Fig. S4** CH<sub>4</sub>-TPR on 111-NiCo<sub>2</sub>O<sub>4</sub>-400 showing CH<sub>4</sub> consumption and evolution of CO<sub>2</sub>, H<sub>2</sub>O, H<sub>2</sub> and CO. The second peak at *ca.* 700 °C occurs from the reduction of M<sup>2+</sup> species to M<sup>0</sup>. The evolution of H<sub>2</sub> and CO in that region are a result of methane cracking due to the presence of M<sup>0</sup> species.<sup>10</sup>

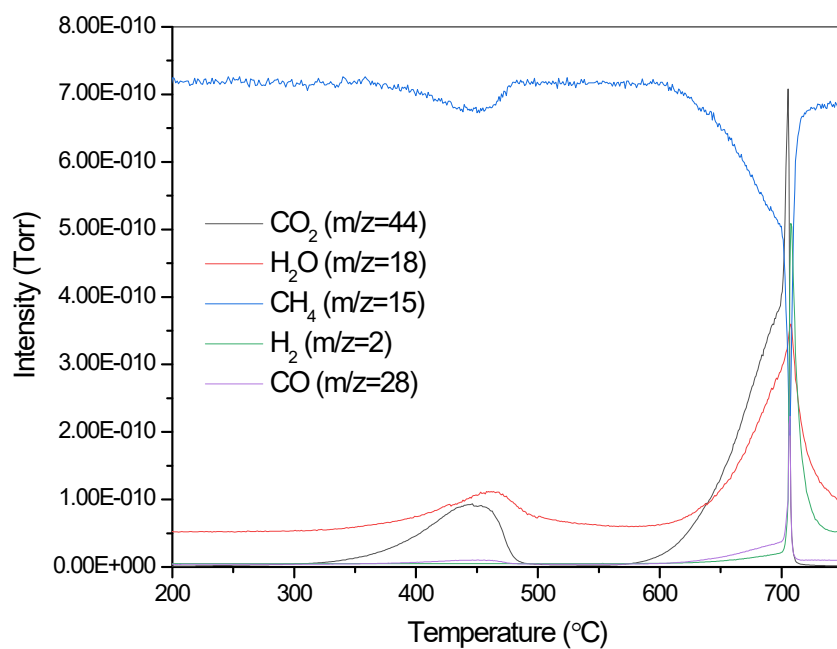


**Fig. S5** CH<sub>4</sub>-TPR on 112-NiCo<sub>2</sub>O<sub>4</sub>-400 showing CH<sub>4</sub> consumption and evolution of CO<sub>2</sub>, H<sub>2</sub>O, H<sub>2</sub> and CO. The second peak at *ca.* 700 °C occurs from the reduction of M<sup>2+</sup> species to M<sup>0</sup>.<sup>7</sup> The evolution of H<sub>2</sub> and CO in that region are a result of methane cracking due to the presence of M<sup>0</sup> species.<sup>10</sup>

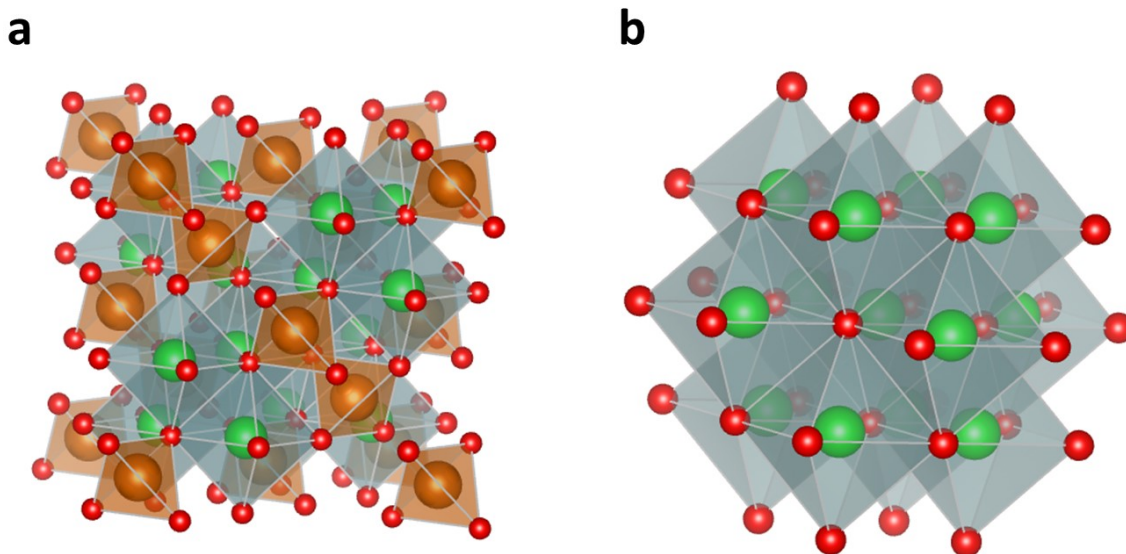


**Fig. S6** Crystalline structure of a)  $\text{NiCo}_2\text{O}_4$  and b)  $\text{NiO}$ . The green, brown and red spheres correspond to Ni, Co and O, respectively.

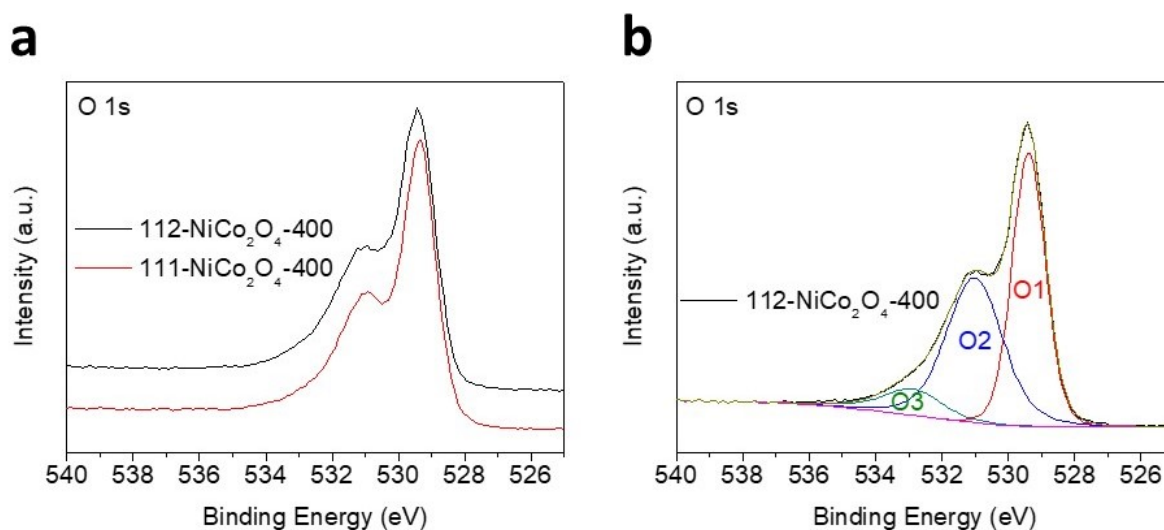


**Fig. S7** a) High resolution XPS scans of O 1s for 111-  $\text{NiCo}_2\text{O}_4$ -400 and 112- $\text{NiCo}_2\text{O}_4$ -400, b) Peak-fitted O 1s high resolution spectrum for 112- $\text{NiCo}_2\text{O}_4$ -400.

The peak-fitted spectra for both samples consist of 3 peaks at *ca.* 529 eV, 531 eV and 531-532 eV respectively (this is shown for sample 112- $\text{NiCo}_2\text{O}_4$ -400 in Figure S7b as an example), which correspond to lattice oxygen (O1), metal hydroxides/hydroxyls (O2) and contributions from organic oxygen (O2, O3), respectively<sup>11-13</sup>. The calculated values for O1, O2 and O3 are presented in Table S1.

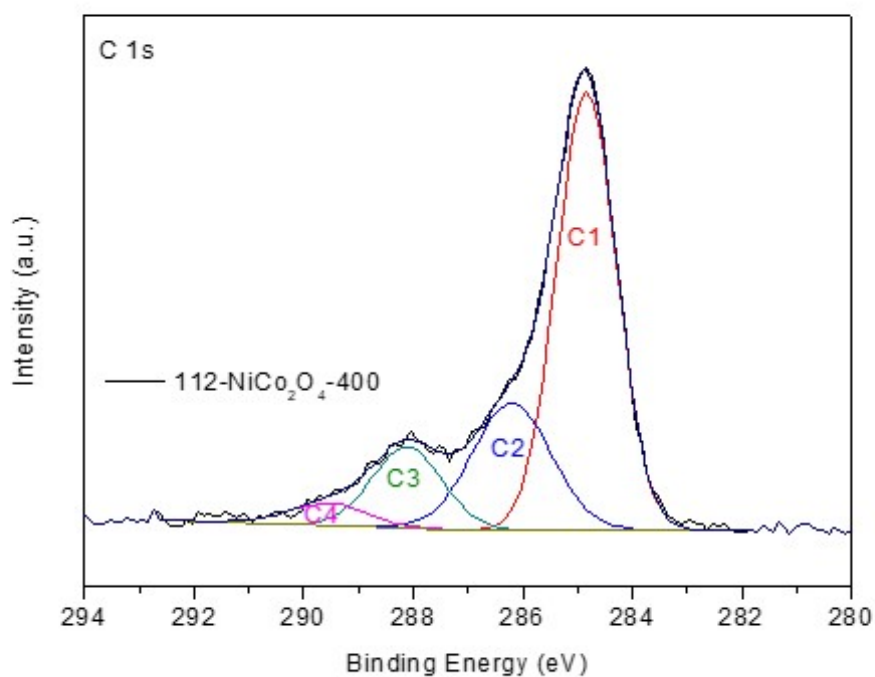
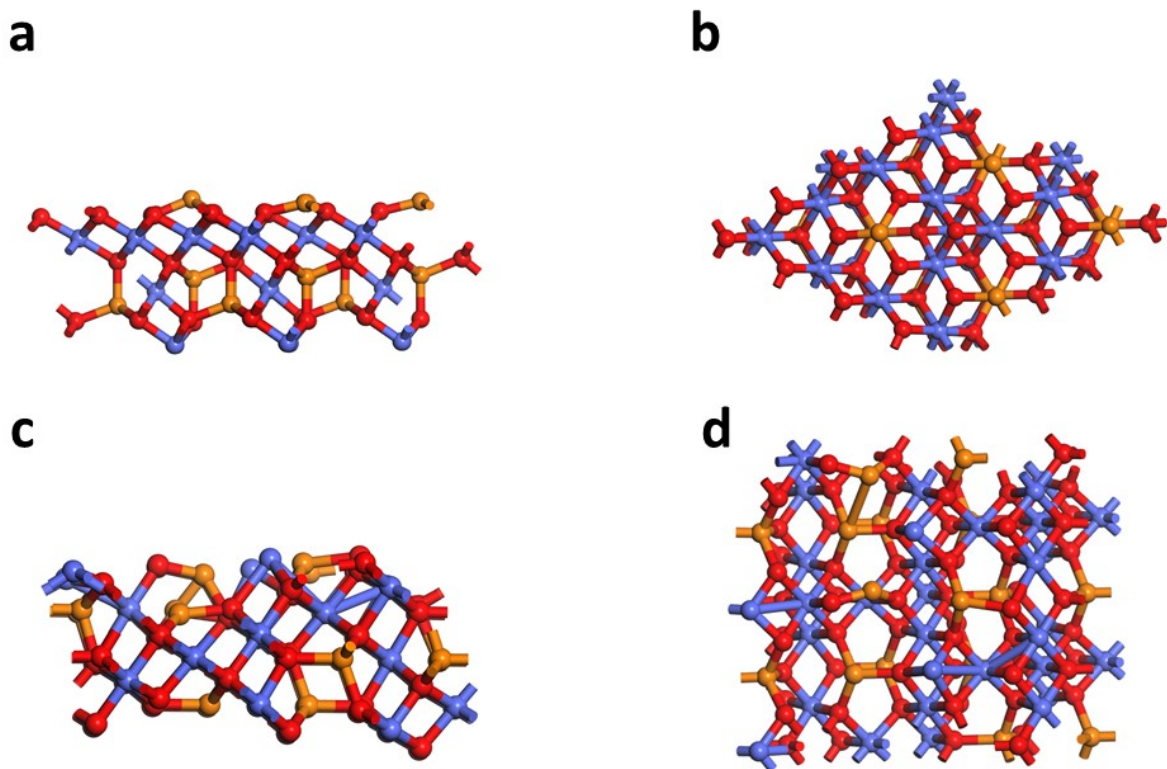


**Fig. S8** Peak-fitted high-resolution C 1s spectrum (XPS) for 112-NiCo<sub>2</sub>O<sub>4</sub>-400.

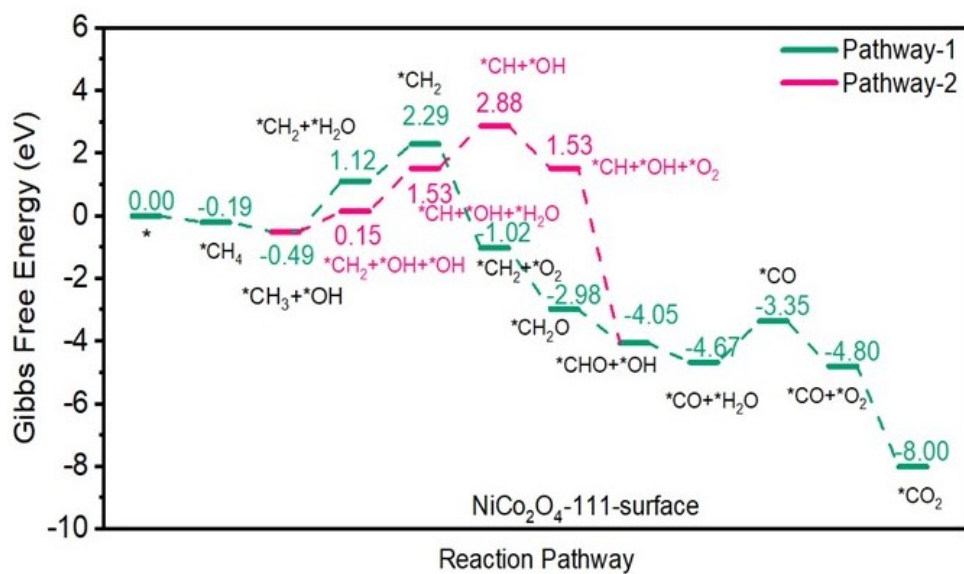
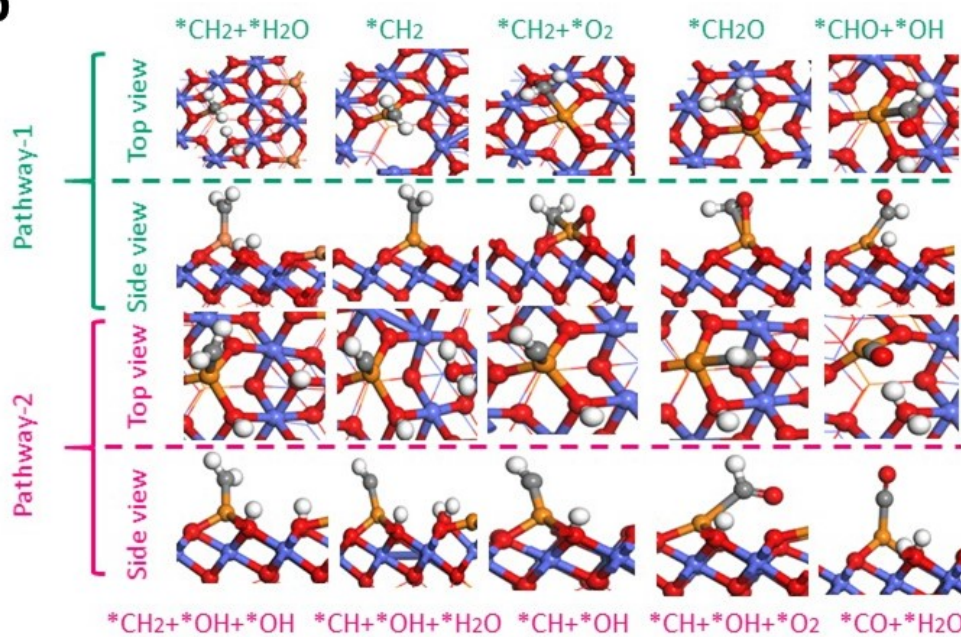
The contribution to the total O 1s signal by organic oxygen, i.e., oxygen bonded to carbon in surface contamination was estimated by fitting C 1s spectra (here we show in Figure S8 an example of a C 1s peak-fit for sample 112-NiCo<sub>2</sub>O<sub>4</sub>-400). The resulting fractions of different carbon-oxygen functional groups resulting from the fits were subsequently converted to an approximate concentration of organic O (see Table S1) using reasonable assumptions regarding the type of functional groups present.

Table S1: Elemental and species quantification of XPS data. Shown are surface compositions, expressed as mean atomic concentration values (+/- deviation) of two measurements per sample. Note that deviations do not correspond to total uncertainties associated with these measurements (see Characterization – XPS experimental details). See text for details.

Sample	111-NiCo <sub>2</sub> O <sub>4</sub> -400 (fresh)		112-NiCo <sub>2</sub> O <sub>4</sub> -400 (fresh)		111-NiCo <sub>2</sub> O <sub>4</sub> -450 (fresh)		112-NiCo <sub>2</sub> O <sub>4</sub> -450 (fresh)		111-NiCo <sub>2</sub> O <sub>4</sub> -450 (spent)		112-NiCo <sub>2</sub> O <sub>4</sub> -450 (spent)	
	Mean	Dev.										
<b>Elemental Compositions (%)</b>												
<b>Ni</b>	<b>21.5</b>	<b>0.2</b>	<b>17.3</b>	<b>0.4</b>	<b>20.5</b>	<b>0.2</b>	<b>17.5</b>	<b>0.3</b>	<b>18.3</b>	<b>0.4</b>	<b>18.2</b>	<b>0.7</b>
<b>Co</b>	<b>21.5</b>	<b>0.1</b>	<b>25.4</b>	<b>0.2</b>	<b>22.0</b>	<b>0.1</b>	<b>24.6</b>	<b>0.2</b>	<b>22.9</b>	<b>0.1</b>	<b>23.3</b>	<b>0.4</b>
<b>O</b>	<b>43.0</b>	<b>0.3</b>	<b>43.4</b>	<b>0.2</b>	<b>43.0</b>	<b>0.6</b>	<b>43.6</b>	<b>0.0</b>	<b>42.6</b>	<b>0.0</b>	<b>41.8</b>	<b>0.0</b>
<b>C</b>	<b>13.7</b>	<b>0.2</b>	<b>13.7</b>	<b>0.2</b>	<b>14.0</b>	<b>0.4</b>	<b>14.3</b>	<b>0.2</b>	<b>15.4</b>	<b>0.4</b>	<b>16.0</b>	<b>0.8</b>
<b>Na</b>	<b>0.3</b>	<b>0.2</b>	<b>0.2</b>	<b>0.2</b>	<b>0.5</b>	<b>0.1</b>	<b>0.0</b>	<b>0.0</b>	<b>0.8</b>	<b>0.1</b>	<b>0.7</b>	<b>0.6</b>
<b>Results of peak fitting (%)</b>												
	<b>Mean</b>	<b>Dev.</b>										
<i>Ni1</i>	<b>18.2</b>	<b>0.4</b>	<b>13.2</b>	<b>0.3</b>	<b>18.3</b>	<b>0.2</b>	<b>14.4</b>	<b>0.1</b>	<b>17.1</b>	<b>0.3</b>	<b>17.0</b>	<b>0.6</b>
<i>Ni2</i>	<b>3.3</b>	<b>0.1</b>	<b>4.1</b>	<b>0.0</b>	<b>2.2</b>	<b>0.1</b>	<b>3.1</b>	<b>0.2</b>	<b>1.2</b>	<b>0.1</b>	<b>1.2</b>	<b>0.0</b>
<i>O1</i>	<b>22.2</b>	<b>0.0</b>	<b>20.6</b>	<b>0.1</b>	<b>22.6</b>	<b>0.3</b>	<b>21.9</b>	<b>0.2</b>	<b>23.3</b>	<b>0.4</b>	<b>23.7</b>	<b>0.4</b>
<i>O2</i>	<b>17.5</b>	<b>0.2</b>	<b>18.9</b>	<b>0.3</b>	<b>17.5</b>	<b>0.3</b>	<b>18.1</b>	<b>0.4</b>	<b>16.4</b>	<b>0.4</b>	<b>15.5</b>	<b>0.7</b>
<i>O3</i>	<b>3.3</b>	<b>0.1</b>	<b>3.9</b>	<b>0.1</b>	<b>2.9</b>	<b>0.0</b>	<b>3.6</b>	<b>0.1</b>	<b>2.9</b>	<b>0.0</b>	<b>2.6</b>	<b>0.3</b>
<i>Organic O</i>	<b>5.9</b>	<b>0.1</b>	<b>6.1</b>	<b>0.2</b>	<b>5.6</b>	<b>0.0</b>	<b>6.0</b>	<b>0.0</b>	<b>5.8</b>	<b>0.0</b>	<b>5.5</b>	<b>0.1</b>
<b>Atomic ratios</b>												
<i>Ni1/Ni2</i>	<b>5.5</b>		<b>3.2</b>		<b>8.3</b>		<b>4.6</b>		<b>14.3</b>		<b>14.2</b>	
<i>Ni/C</i>	<b>1.0</b>		<b>0.7</b>		<b>0.9</b>		<b>0.7</b>		<b>0.8</b>		<b>0.8</b>	



**Fig. S9** (a) (b) The side and top view of the optimized structure for NiCo<sub>2</sub>O<sub>4</sub> (111) surface, (c) (d) The side and top view for NiCo<sub>2</sub>O<sub>4</sub> (112) surface. The blue, red and orange balls represent Co, O and Ni atoms, respectively.

**a****b**

**Fig. S10** a) Gibbs free energy diagram showing pathways and b) selected molecular conformations for CH<sub>4</sub> oxidation on the 111-NiCo<sub>2</sub>O<sub>4</sub> surface.

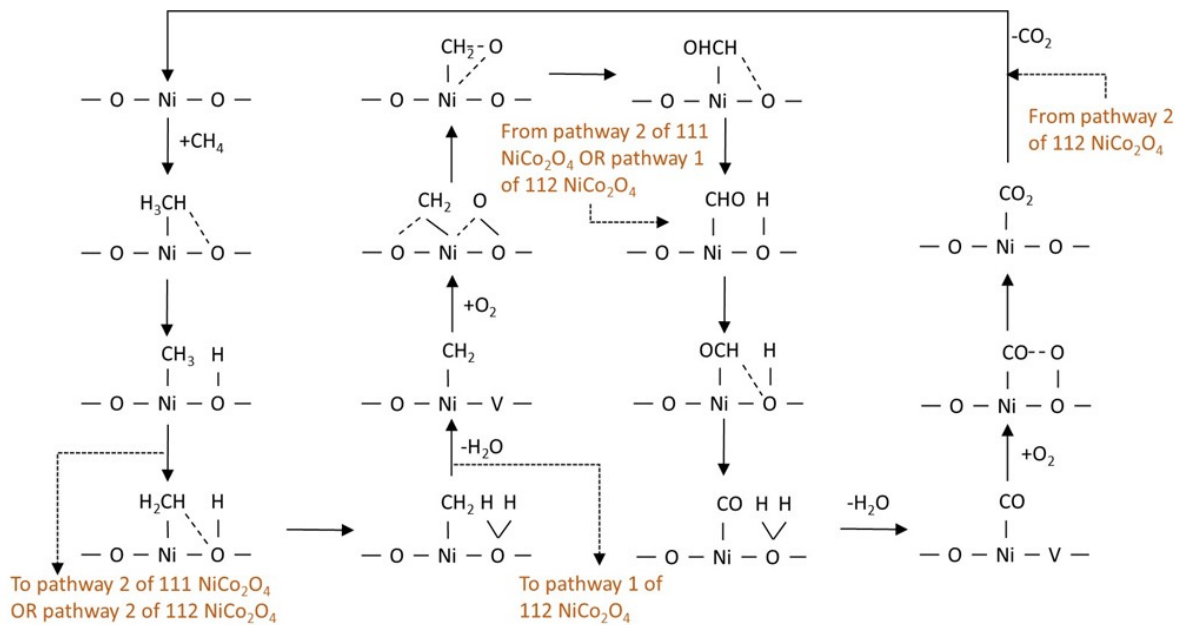


**Fig. S11** Pathway 1 of the reaction mechanism of methane oxidation on 111-NiCo<sub>2</sub>O<sub>4</sub>.

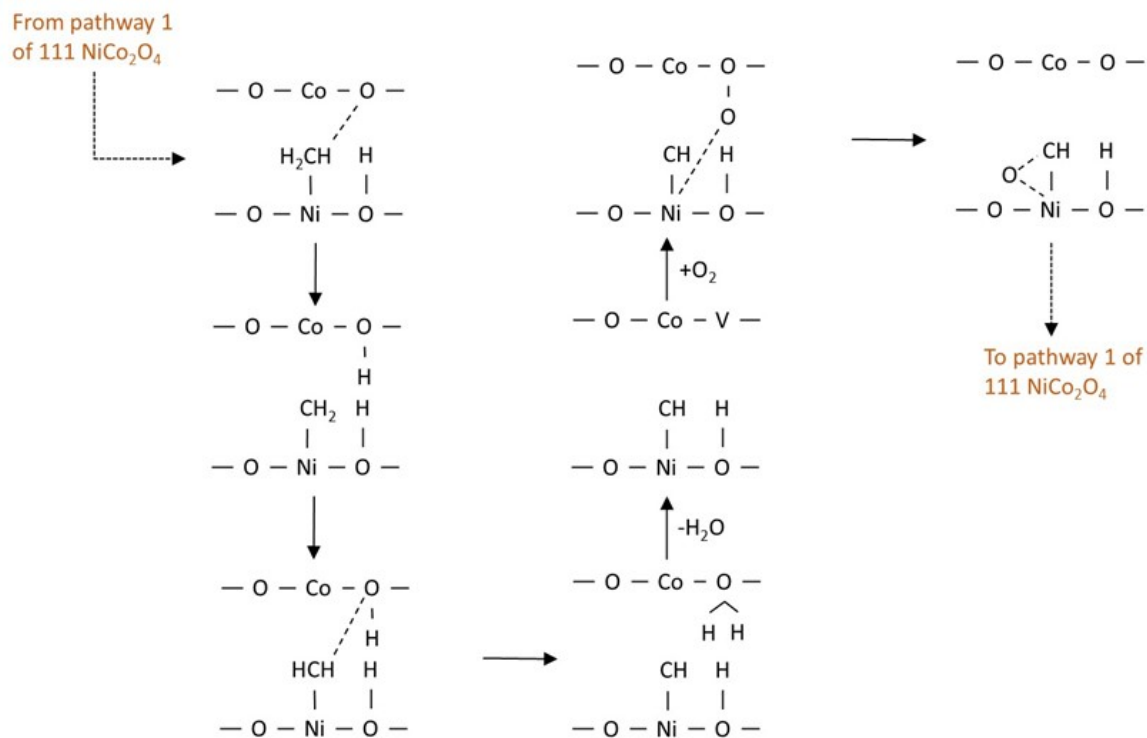


**Fig. S12** Pathway 2 of the reaction mechanism of methane oxidation on 111-NiCo<sub>2</sub>O<sub>4</sub>.

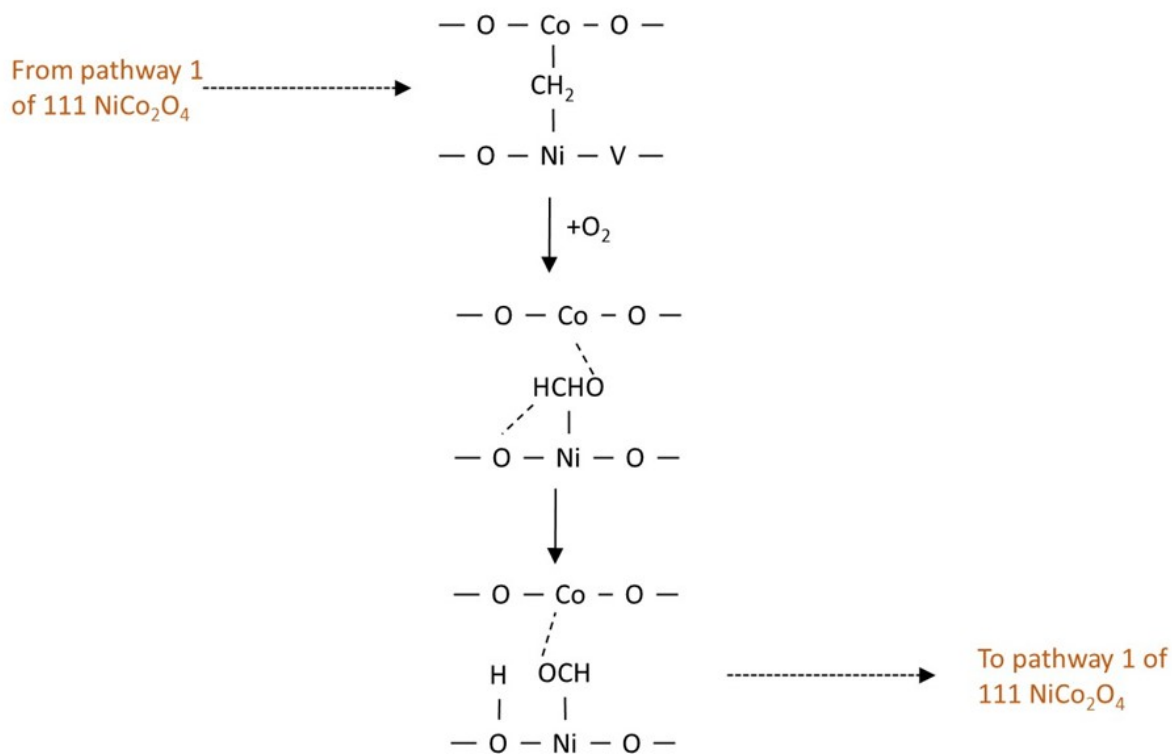


**Fig. S13** Pathway 1 of the reaction mechanism of methane oxidation on 112-NiCo<sub>2</sub>O<sub>4</sub>.

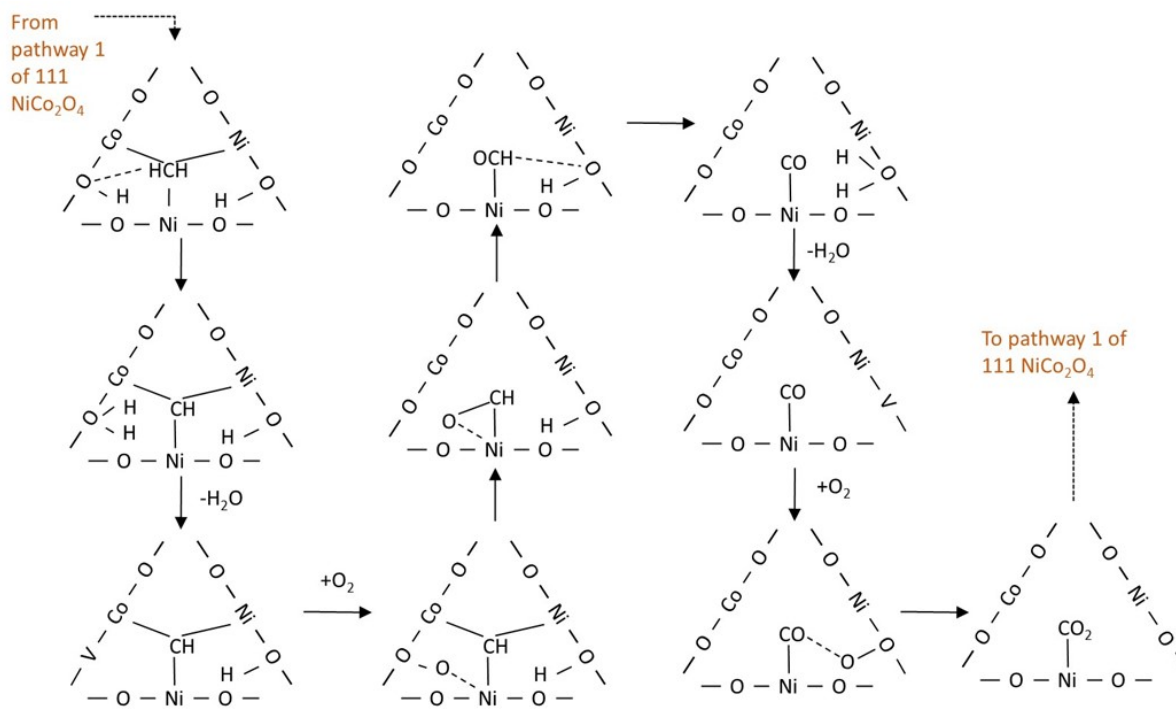


**Fig S14** Pathway 2 of the reaction mechanism of methane oxidation on 112-NiCo<sub>2</sub>O<sub>4</sub>.

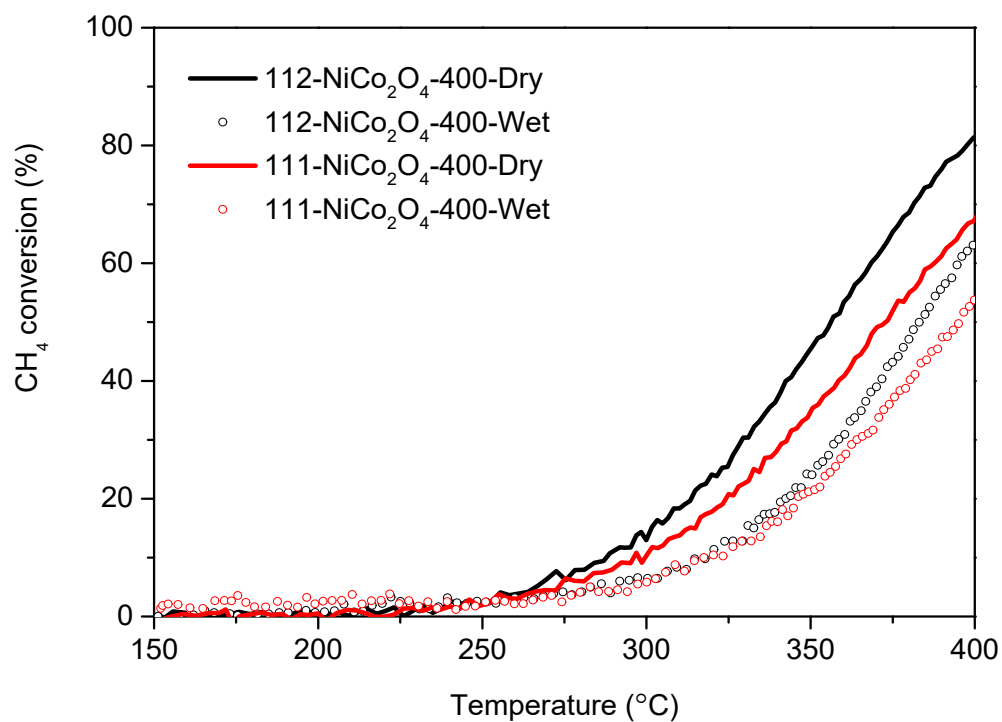


**Fig S15** Light-off curves (truncated to reaction temperature of 400 °C) of methane oxidation under dry and wet conditions for 111- NiCo<sub>2</sub>O<sub>4</sub>-400 and 112-NiCo<sub>2</sub>O<sub>4</sub>-400.

Table S2: DFT calculated adsorption and activation energies of water on 111-NiCo<sub>2</sub>O<sub>4</sub> and 112-NiCo<sub>2</sub>O<sub>4</sub> surfaces.

Surface	H <sub>2</sub> O adsorption energy (eV)	H <sub>2</sub> O activation barrier (eV) *H <sub>2</sub> O+*→*OH+*H process
112 surface	-1.59 (Co site) -0.52 (Ni site)	0.84
111 surface	-0.94 (Ni site)	0.66

Table S3: DFT calculated adsorption and activation energies of methane on 111-NiCo<sub>2</sub>O<sub>4</sub> and 112-NiCo<sub>2</sub>O<sub>4</sub> surfaces.

Surface	CH <sub>4</sub> adsorption energy (eV)	CH <sub>4</sub> activation barrier (eV) *CH <sub>4</sub> +*→*CH <sub>3</sub> +*H process
112 surface	-0.3	0.92
111 surface	-0.19	0.96

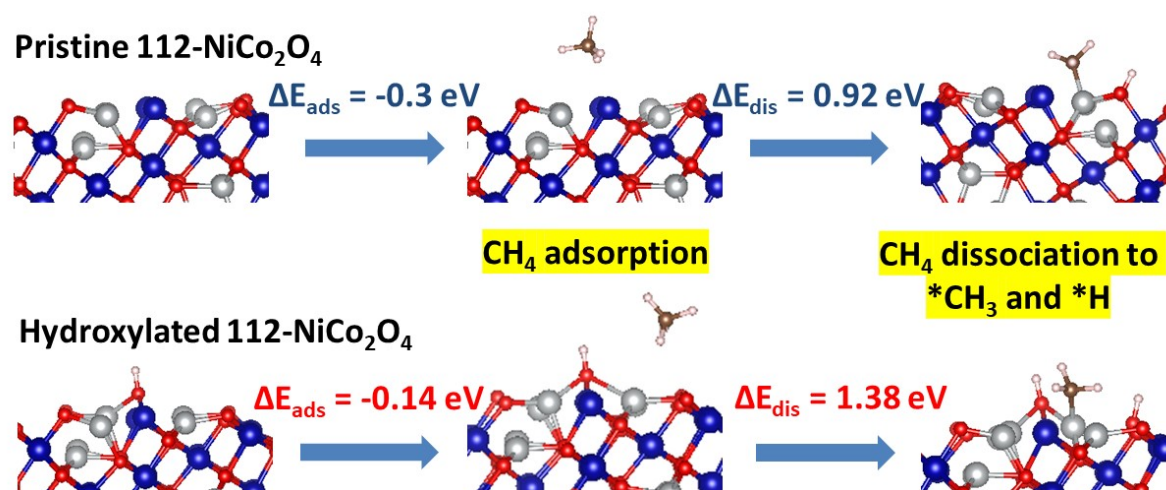
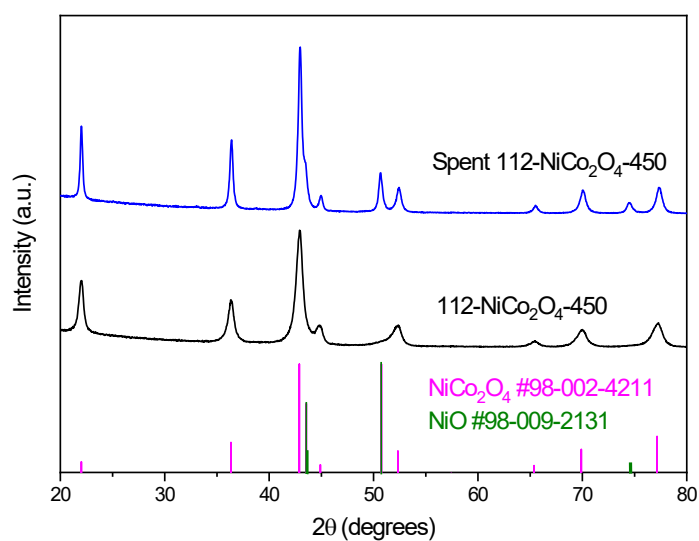
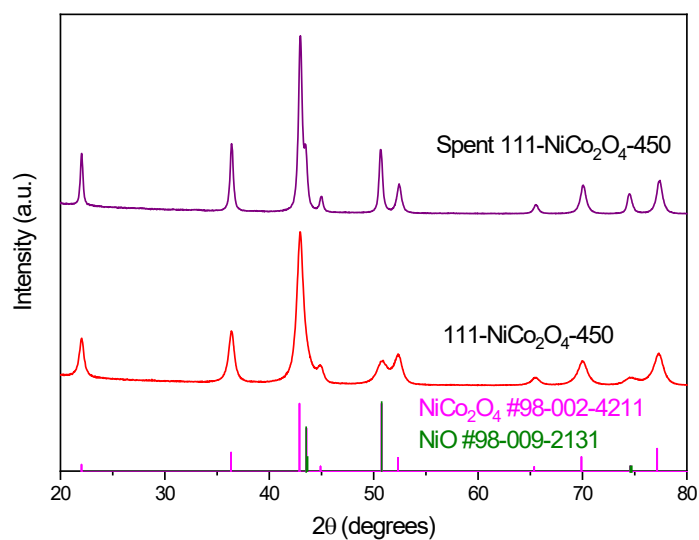


Fig. S16 DFT simulations comparing the adsorption and dissociation of methane on pristine and hydroxylated 112-NiCo<sub>2</sub>O<sub>4</sub>.



**Fig. S17** XRD patterns of fresh and spent 112-NiCo<sub>2</sub>O<sub>4</sub>-450 (after *ca.* 66 h stability testing at 500 °C and 3.2% humidity).



**Fig. S18** XRD patterns of fresh and spent 111-NiCo<sub>2</sub>O<sub>4</sub>-450 (after *ca.* 66 h stability testing at 500 °C and 3.2% humidity).

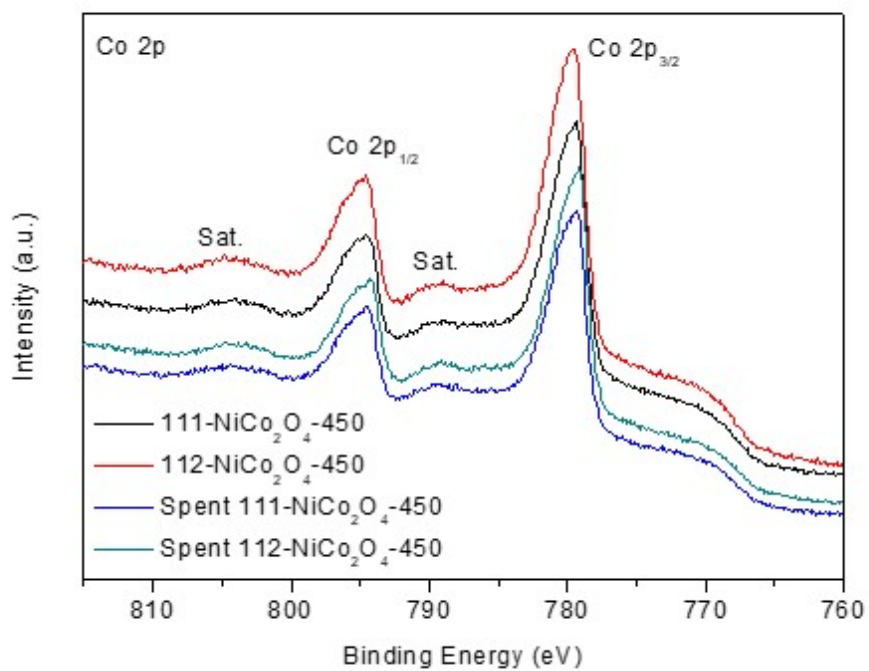


**Fig. S19** High resolution Co 2p XP spectrum for fresh and spent 111-NiCo<sub>2</sub>O<sub>4</sub>-450 and 112-NiCo<sub>2</sub>O<sub>4</sub>-450.

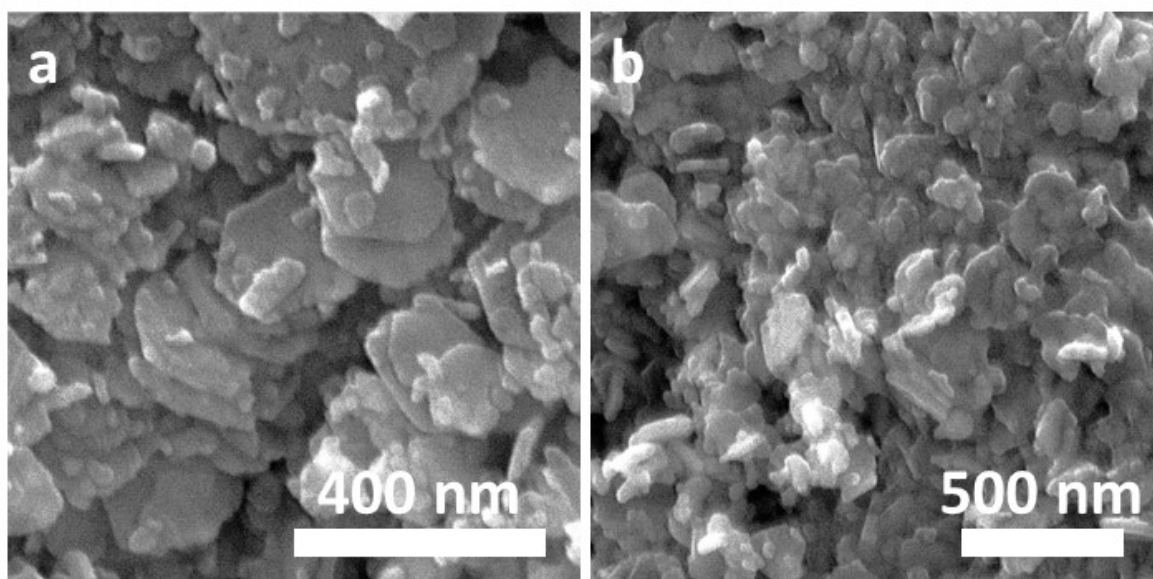


**Fig. S20** SEM image of a) 111-NiCo<sub>2</sub>O<sub>4</sub>-450 and b) spent 111-NiCo<sub>2</sub>O<sub>4</sub>-450.

Table S4: Comparison of this work's catalyst performance with similar materials from published data.

<b>Catalyst</b>	<b>Experimental conditions</b>	<b>Performance</b>	<b>Reference</b>
Co <sub>3</sub> O <sub>4</sub> /CeO <sub>2</sub> nanocomposite	WHSV = 9000 mL g <sup>-1</sup> h <sup>-1</sup> , dry conditions.	T <sub>50</sub> = 475 °C T <sub>100</sub> <i>ca.</i> 600 °C	14
Hydrothermal 60 h NiCo <sub>2</sub> O <sub>4</sub>	420 °C GHSV = 24000 mL h <sup>-1</sup> g <sup>-1</sup> with 10 vol% H <sub>2</sub> O.	<i>ca.</i> 90% activity maintained after 12 h.	15
Core-shell NiO@PdO nanoparticles (0.2 wt% Pd)	GHSV = 30 000 mL h <sup>-1</sup> g <sup>-1</sup> , 6-9 vol% H <sub>2</sub> O.	T <sub>99</sub> = 400. 92% activity retained after 50 h.	16
Bowtie-shaped NiCo <sub>2</sub> O <sub>4</sub> nanostructures	(GHSV): 90 000 mL (STP) g <sup>-1</sup> h <sup>-1</sup> , dry conditions.	100% conversion at ≈ 410 °C.	17
NiCo <sub>2</sub> O <sub>4</sub> nanoparticles	(GHSV): 24 000 mL (STP) g <sup>-1</sup> h <sup>-1</sup> , 5% CH <sub>4</sub> , dry conditions.	100% conversion for 48 h at 350 °C and 550.	18
1wt%Pd-NiCo <sub>2</sub> O <sub>4</sub>	1 vol.% CH <sub>4</sub> in air and dry conditions; GHSV = 30,000 mL h <sup>-1</sup> g <sup>-1</sup> cat.	T <sub>90</sub> = 344 °C. <i>ca.</i> 85% activity retained after 200 h at 350 °C.	19
112-NiCo <sub>2</sub> O <sub>4</sub> -400	0.7 vol.% CH <sub>4</sub> in 15.0 vol % O <sub>2</sub> and balance Ar and 3.2% water vapour; GHSV = 40,000 mL h <sup>-1</sup> g <sup>-1</sup> cat.	T <sub>90</sub> = 500 °C. <i>ca.</i> 86% activity retained after 230 h at 500 °C and 3.2% water vapour.	<b><i>This work.</i></b>

## References

1. H. Wang, Tailoring Cathode Nanostructures for Performance Improvement of Non-Aqueous Lithium-Oxygen Batteries, Ph.D. diss., *University of Adelaide*, 2019.
2. G. Kresse and J. Furthmuller, *Physical Review B*, 1996, **54**, 11169-11186.
3. G. Kresse and J. Furthmuller, *Computational Materials Science*, 1996, **6**, 15-50.
4. J. Perdew, K. Burke and M. Ernzerhof, *Physical Review Letters*, 1996, **77**, 3865-3868.
5. J. Perdew, M. Ernzerhof and K. Burke, *Journal of Chemical Physics*, 1996, **105**, 9982-9985.
6. S. Grimme, *Journal of Computational Chemistry*, 2006, **27**, 1787-1799.
7. G. Henkelman and H. Jónsson, *Journal of Chemical Physics*, 2000, **113**, 9978-9985.
8. G. Henkelman, B. Uberuaga and H. Jónsson, *Journal of Chemical Physics*, 2000, **113**, 9901-9904.
9. D. Su, S. Dou and G. Wang, *Scientific reports*, 2014, **4**, 5767.
10. L. Hu, Q. Peng and Y. Li, *Journal of the American Chemical Society*, 2008, **130**, 16136-16137.
11. M. Biesinger, B. Payne, A. Grosvenor, L. Lau, A. Gerson and R. Smart, *Applied Surface Science*, 2011, **257**, 2717-2730.
12. M. Biesinger, B. Payne, L. Lau, A. Gerson and R. Smart, *Surface and Interface Analysis*, 2009, **41**, 324-332.
13. H. Idriss, *Surface Science*, 2021, **712**, 121894.
14. J. Dou, Y. Tang, L. Nie, C.M. Andolina, X. Zhang, S. House, Y. Li, J. Yang and F.F. Tao, *Catalysis Today*, 2018, **311**, 48-55.
15. Z. Zhang, J. Li, T. Yi, L. Sun, Y. Zhang, X. Hu, W. Cui and X. Yang, *Chinese Journal of Catalysis*, 2018, **39**, 1228-1239.
16. X. Zou, Z. Rui and H. Ji, *ACS Catalysis*, 2017, **7**, 1615-1625.
17. Y. Dai, V.P. Kumar, C. Zhu, H. Wang, K.J. Smith, M.O. Wolf and M.J. MacLachlan, *Advanced Functional Materials*, 2019, **29**, 1807519.
18. F.F. Tao, J.J. Shan, L. Nguyen, Z. Wang, S. Zhang, L. Zhang, Z. Wu, W. Huang, S. Zeng and P. Hu, *Nature communications*, 2015, **6**, 7798.
19. T. Wang, L. Qiu, H. Li, C. Zhang, Y. Sun, S. Xi, J. Ge, Z.J. Xu and C. Wang, *Journal of Catalysis*, 2021, **404**, 400-410.